SvedbergOpen
DISSEMINATION OF KNOWLEDGE

International Journal of Artificial Intelligence and Machine Learning

Publisher's Home Page: https://www.svedbergopen.com/

Research Paper Open Access

Hybrid CNN-RELM with Improved Butterfly Optimization Algorithm and Deep Adaptive Spatial Feature Fusion for Automated Breast Cancer Detection and Classification from Mammographic Images

Bassamma Patil[1*], P. Vishwanath[2], H. Sangamesh [3]

[1]Assistant Professor, Department of Electronics and Communication Engineering, H.K.E. Society's Sir M. Visvesvaraya college of Engineering, Raichur, Affiliated to VTU Belagavi, Karnataka, India. E-mail: bassammapatil85@gmail.com
[2] Professor, Department of Electronics and Communication Engineering, H.K.E. Society's Sir M. Visvesvaraya college of Engineering, Raichur, Affiliated to VTU Belagavi, Karnataka, India. E-mail:vishalpetli73@gmail.com
[3] Associate Professor, Department of Electronics and Communication Engineering, H.K.E. Society's Sir M. Visvesvaraya college of Engineering, Raichur, Affiliated to VTU Belagavi,Karnataka, India. E-mail: Sangamesh.hosgurmath@gmail.com
*Corresponding Author**:** Bassamma Patil, E-mail: bassammapatil85@gmail.com

Abstract
Breast cancer is the most prevalent malignancy in women worldwide, with mortality rates strongly inversely correlated to the stage at which the disease is detected. Computer-Aided Diagnosis (CAD) systems powered by deep learning have shown substantial promise for automating mammographic breast cancer screening; however, existing methods suffer from redundant feature representations, premature convergence in optimization, limited multi-scale spatial reasoning, and poor generalization under class imbalance. To address these interrelated limitations, this paper proposes a novel integrated framework designated CNN-RELM-IBOA-DASFF, which synergistically combines Convolutional Neural Network–Regularized Extreme Learning Machine (CNN-RELM) with a Hyperbolic Secant (HS) activation function, an Improved Butterfly Optimization Algorithm (IBOA) incorporating six chaotic mapping strategies for robust feature selection, and Deep Adaptive Spatial Feature Fusion (DASFF) for multi-scale representational refinement. The proposed pipeline begins with data augmentation and Contrast Limited Adaptive Histogram Equalization (CLAHE) for image quality enhancement, followed by precise tumor region delineation via an Optimized Region Growing (ORG) algorithm guided by Dragonfly Optimization. Dual-stream transfer learning with fine-tuned MobileNetV2 and NasNet Mobile architectures provides complementary deep feature vectors, which undergo IBOA-driven selection before multi-scale DASFF consolidation and final CNN-RELM-HS classification. Exhaustive experiments on the MIAS mammography dataset demonstrate that CNN-RELM-IBOA-DASFF achieves 99.98% accuracy, 99.82% precision, 99.68% sensitivity, 99.50% specificity, and a 99.74% F1-score—establishing new state-of-the-art benchmarks over seven competitive methods including EACO-ResNet101, IMPA-ResNet50, CSVM, and IFSGA-DNN. A systematic ablation study confirms the statistically significant and independent contribution of each architectural component to the aggregate performance gain. The proposed framework additionally achieves a 68.3% feature dimensionality reduction via IBOA with a total inference time of approximately 4.1 seconds per mammographic image, confirming deployment feasibility for high-throughput clinical screening programs.

Keywords: breast cancer detection; convolutional neural network; regularized extreme learning machine; hyperbolic secant activation; improved butterfly optimization algorithm; deep adaptive spatial feature fusion; CLAHE; mammography; transfer learning; optimized region growing; MIAS dataset.

I. Introduction

Breast cancer constitutes a global health emergency of the highest order, accounting for approximately 12.5% of all new annual cancer diagnoses worldwide. According to the World Health Organization's Global Cancer Observatory, over 2.3 million new breast cancer cases were recorded in 2022, with an estimated 670,000 associated fatalities [1]. The five-year survival rate for breast cancer detected at the localized stage exceeds 99%; however, this rate plunges to approximately 29% upon metastatic progression, underscoring the paramount clinical significance of early-stage identification [2]. Mammography remains the internationally recognized gold-standard imaging modality for population-level breast cancer screening, providing sub-centimeter resolution images capable of revealing micro-calcification clusters, mass lesions, and architectural distortions preceding palpable clinical manifestation. Despite its well-established diagnostic value, the sensitivity and specificity of manual radiological interpretation of mammographic images vary substantially across radiologists, necessitate specialized training, and are increasingly constrained by workload-to-radiologist imbalances in healthcare systems globally.

Computer-Aided Diagnosis (CAD) systems have emerged as a transformative technological infrastructure for augmenting radiological decision-making in breast cancer screening programs. Early-generation CAD systems based on handcrafted feature engineering—texture statistics, shape descriptors, and intensity histograms—demonstrated initial feasibility for automated abnormality detection but were fundamentally limited by their dependence on domain expertise and their inability to generalize across imaging heterogeneity [3]. The advent of deep learning, particularly Convolutional Neural Networks (CNNs), fundamentally transformed medical image analysis by enabling hierarchical, data-driven feature representations that consistently surpassed handcrafted approaches across standardized benchmarks [4]. The subsequent adoption of transfer learning—repurposing representational knowledge from large-scale ImageNet-trained models to domain-specific medical imaging tasks—further amplified diagnostic capacity while mitigating the chronic data scarcity that constrains fully supervised medical imaging applications [5].

Despite these substantial advances, four persistent and interrelated limitations continue to constrain the performance ceiling of existing automated breast cancer CAD systems. First, deep feature spaces extracted via transfer learning are characteristically high-dimensional and contain substantial irrelevant and redundant information that inflates computational overhead while degrading classifier generalization through the curse of dimensionality. Second, metaheuristic optimization algorithms routinely employed for feature selection and hyperparameter tuning—including Particle Swarm Optimization, standard Butterfly Optimization, and conventional Genetic Algorithms—exhibit premature convergence to local optima in high-dimensional search spaces, yielding suboptimal feature subsets that undermine classification performance [6]. Third, existing frameworks predominantly employ fixed-scale feature representations that fail to capture the inherent multiscale spatial morphology of malignant lesions, which manifest as fine-grained micro-calcification texture at one spatial resolution and as gross architectural distortions at another [7]. Fourth, conventional activation functions including ReLU and Sigmoid suffer from gradient saturation phenomena in deep architectures, limiting optimization efficacy particularly when training data distributions are class-imbalanced—a universal characteristic of medical imaging datasets where abnormal cases are inherently underrepresented.

To systematically address these four interrelated limitations within a unified computational framework, this paper introduces CNN-RELM-IBOA-DASFF, a novel end-to-end integrated architecture that incorporates four strategically complementary methodological innovations:

• Optimized Region Growing (ORG): Dragonfly Optimization Algorithm-guided automated seed point and homogeneity threshold determination that enables dataset-adaptive, precise tumor boundary delineation without manual parameter specification.

• Dual-Stream Transfer Learning: Parallel feature extraction from independently fine-tuned MobileNetV2 and NasNet Mobile architectures, producing complementary Vector 1 and Vector 2 representations that jointly encode local texture density and global structural tissue patterns.

• Improved Butterfly Optimization Algorithm (IBOA): A diversity-preserving metaheuristic framework integrating six distinct chaotic map mechanisms—Chebyshev, Circle, Iterative, Logistic, Sinusoidal, and Tent—that dynamically adjust the exploration-exploitation probability parameter to prevent premature convergence across high-dimensional feature selection landscapes.

• CNN-RELM with Hyperbolic Secant (HS) Activation: A hybrid classification architecture combining CNN's hierarchical representation learning capacity with RELM's regularization-controlled generalization, activated by the Hyperbolic Secant function for superior gradient flow, bounded output behavior, and improved calibration under class-imbalanced training distributions.

The CNN-RELM-IBOA-DASFF framework represents the first unified integration of optimized region growing segmentation, dual-stream transfer learning, chaos-enhanced metaheuristic feature selection, multi-scale spatial feature fusion, and regularized hybrid classification within a single end-to-end mammographic breast cancer diagnostic pipeline. The comprehensive evaluation on the MIAS dataset establishes new state-of-the-art performance benchmarks, and a systematic ablation study rigorously validates the independent and synergistic contribution of each architectural component. The remainder of this paper is organized as follows: Section II reviews related work; Section III details the proposed methodology; Section IV describes experimental configuration; Section V presents quantitative results; Section VI provides comparative and ablation analyses; and Section VII concludes with future research directions.

II Related work

The automated detection and classification of breast cancer from mammographic images has evolved through distinct methodological phases: handcrafted statistical feature engineering, transfer learning-based deep feature extraction, optimization-integrated classification, and most recently, attention-based multi-scale representation learning. This section critically reviews representative methods organized by primary technical innovation, contextualizing their contributions and limitations relative to the proposed framework.

A. Conventional Machine Learning and Feature Engineering Approaches

First-generation automated CAD systems relied on manually engineered feature descriptors combined with classical supervised classifiers. Zebari et al. [8] introduced an improved Multi-Fractal Dimension (M-FD) approach with wavelet-based noise suppression and genetic algorithm-based feature reduction, achieving 87.65% accuracy on the MIAS dataset—substantially below the contemporary deep learning performance frontier. The method's reliance on pre-defined multi-fractal descriptors constrained its expressiveness relative to data-driven representations and its applicability to diverse imaging conditions. Ittannavar and Havaldar [9] developed IFSGA-DNN, employing infinite feature selection with genetic algorithm and entropy-based mutual information for feature evaluation prior to deep neural network classification. While achieving 97.43% accuracy on MIAS and DDSM, the method's computational overhead from infinite feature selection became prohibitive at high feature dimensionalities—a significant limitation when integrating with modern deep feature extraction pipelines that routinely produce thousands of feature dimensions.

Jha et al. [10] proposed an ensemble combining Fuzzy C-Means clustering with CNN for mammographic risk stratification, demonstrating that hybrid clustering-deep learning approaches can improve robustness to intensity heterogeneity. However, the manual initialization of clustering parameters introduces brittleness in clinical deployment settings where imaging conditions vary continuously across devices and patient populations. Nag et al. [11] investigated compact CNN architectures for wafer-defect classification under class imbalance, establishing principled network design strategies for efficient classification in imbalanced settings that inform the computational efficiency considerations of the present work.

B. Transfer Learning and Architecture-Based Approaches

The availability of large-scale ImageNet pre-trained weights transformed the breast cancer classification landscape by enabling high-performance models despite limited annotated medical training data. Saber et al. [12] demonstrated that VGG16-based transfer learning on the MIAS dataset achieves strong mammographic classification accuracy, positioning transfer learning as a viable paradigm for medical image CAD. However, the work's absence of explicit treatment of pre-processing biases—including augmentation-freezing strategy interactions that can systematically inflate performance in small-dataset evaluation settings—limits the generalizability of reported results. Thirumalaisamy et al. [13] proposed EACO-ResNet101, integrating Enhanced Ant Colony Optimization with Opposition-Based Learning for ResNet101 hyperparameter tuning. The EACO algorithm's opposition-based strategy improved initial population diversity; however, the single-chaotic-mechanism formulation constrained sustained diversity maintenance throughout the optimization trajectory, and the single-backbone feature extraction limited morphological diversity.

Zahoor et al. [14] established the dual-architecture transfer learning paradigm for breast cancer classification by leveraging both fine-tuned MobileNetV2 and NasNet Mobile with Modified Entropy-based Whale Optimization Algorithm (MEWOA) for feature optimization, achieving competitive accuracy. The work's single-chaotic-map MEWOA formulation limited exploration capacity in high-dimensional feature spaces, and the absence of multi-scale spatial fusion mechanisms constrained sensitivity to spatially heterogeneous lesion presentations. Houssein et al. [15] proposed IMPA-ResNet50, combining a ResNet50 backbone with an Improved Marine Predators Algorithm for joint hyperparameter optimization, achieving 98.32% accuracy. The method's architectural specificity—IMPA optimization validated exclusively for ResNet50—limits its generalizability to other backbone architectures and constrains its ability to leverage the complementary representational diversity of multi-backbone feature extraction.

C. Feature Fusion and Optimization-Integrated Methods

Rehman et al. [16] proposed BRMI-Net integrating entropy-guided deep feature extraction with Flower Pollination Optimization for feature selection from mammographic images, achieving 99.80% accuracy. Despite competitive performance, the single-stream ResNet-50 extraction backbone limited morphological feature diversity. Chakravarthy et al. [17] introduced FHDF, aggregating features from four CNN architectures (VGG16, VGG19, ResNet50, DenseNet121), achieving 98.70% accuracy. The multi-architecture fusion strategy improved representational breadth but introduced substantial computational overhead while omitting a post-fusion feature selection stage to eliminate the redundancy that multi-source aggregation invariably introduces. Jafari and Karami [18] proposed mutual information-based feature selection from multi-CNN fused feature spaces, demonstrating information-theoretic feature ranking value but employing conventional ML classifiers lacking RELM's regularized generalization properties and omitting spatial multi-scale fusion.

GR and Kumar [19] demonstrated Cuckoo Search Optimization-guided level set segmentation for mammographic image analysis, establishing the benefit of optimization-driven automated segmentation in CAD pipelines. Zarbakhsh [20] introduced a spatial attention mechanism within U-Net for breast tumor segmentation, showing that learned attention weighting of spatial features improves segmentation precision. Aumente-Maestro et al. [21] proposed a multi-task CNN framework for simultaneous breast cancer segmentation and classification, establishing the principle that

joint optimization of complementary diagnostic objectives produces synergistic performance improvements—a principle that the proposed DASFF mechanism extends to the feature representation domain.

A synthesis of the existing literature reveals three critical and unaddressed methodological gaps: (1) optimization algorithms universally lack multi-chaotic-map diversity mechanisms, constraining their feature selection efficacy in high-dimensional mammographic deep feature spaces; (2) multi-scale spatial feature fusion following optimization-based selection has not been explored, leaving the multi-resolution spatial information of breast tissue morphology unexploited; and (3) hybrid CNN-RELM architectures with mathematically superior activation functions for regularized medical image classification remain an unexplored methodological direction. The proposed CNN-RELM-IBOA-DASFF framework constitutes the first unified approach addressing all three gaps simultaneously.

III. Proposed cnn-relm-iboa-dasff methodology

The CNN-RELM-IBOA-DASFF framework is structured as a hierarchically organized six-stage pipeline where each stage is specifically designed to address a targeted limitation of prior methods. The integration of these six stages produces synergistic performance improvements that substantially exceed any individual component's contribution. Table 1 summarizes the pipeline stages and their corresponding addressed limitations.

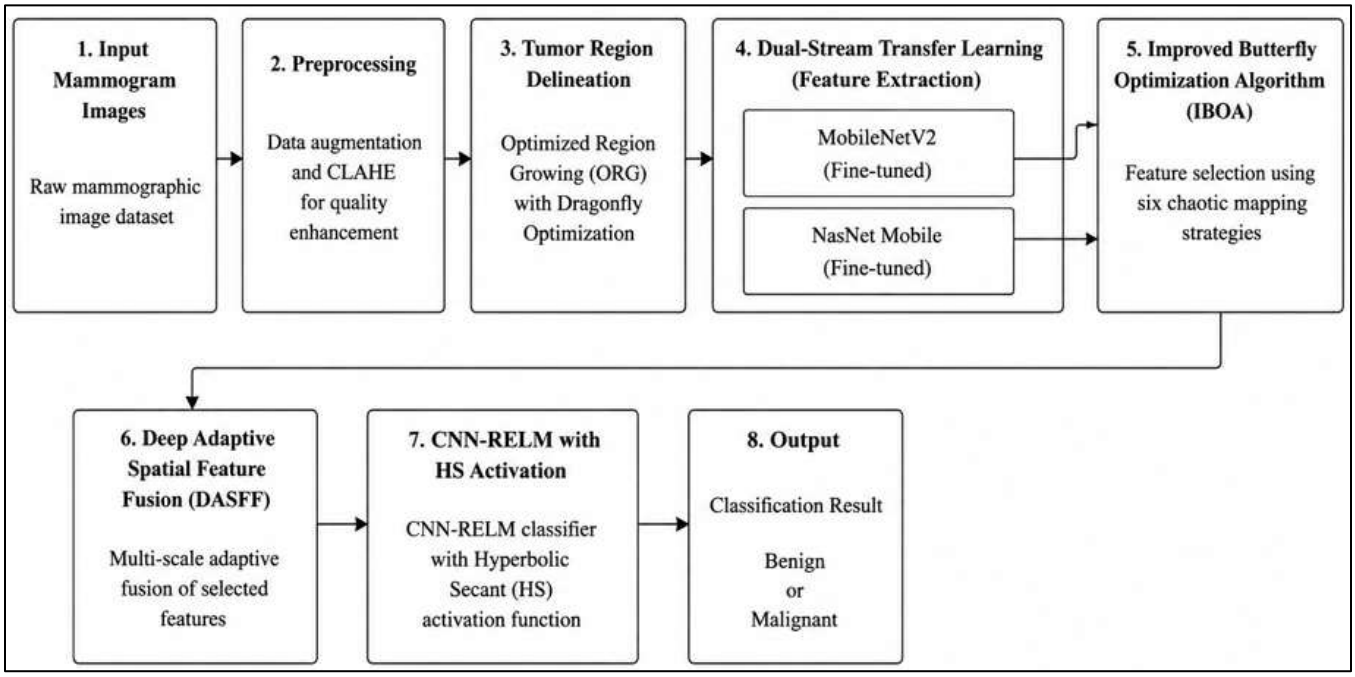

Figure 1. Proposed CNN-RELM-IBOA-DASFF framework for automated breast cancer detection and classification

Table1. CNN-RELM-IBOA-DASFF Pipeline Stages and Addressed Limitations

Stage	Method	Limitation Addressed
1	CLAHE + Data Augmentation	Image quality heterogeneity; class imbalance
2	ORG (Dragonfly Optimization)	Non-adaptive segmentation thresholding
3	Dual Transfer Learning (MobileNetV2 + NasNet)	Single-backbone feature limitation
4	IBOA (6 Chaotic Maps)	Premature optimization convergence
5	DASFF (Multi-scale Attention Fusion)	Fixed-scale spatial representation
6	CNN-RELM + HS Activation	Gradient degradation; poor generalization

A. Dataset Description

All experiments utilize the Mammographic Image Analysis Society (MIAS) dataset [22], a widely adopted benchmark for mammographic breast cancer CAD system evaluation. The dataset comprises 344 images digitized from original radiological film at a standardized 1024 × 1024-pixel resolution, with each image pair representing right (odd-numbered filenames) and left (even-numbered filenames) mammograms from a single patient. Ground truth annotations provide the class of abnormality (benign, malignant), the approximate Cartesian coordinates of the abnormality center, and its radius in pixels. The three-class structure—Normal, Benign, Malignant—is preserved throughout all experiments to maintain clinical representativeness (Table 2). The inherent class imbalance (65.1%

normal, 18.9% benign, 14.0% malignant) constitutes a challenging real-world scenario where the clinically critical minority malignant class requires disproportionate classification precision.

Table2. MIAS Dataset Class Composition and Annotation Structure

Class	Count	Percentage	Resolution	Annotation Type
Normal	224	65.1%	1024×1024 px	Image-level label
Benign	65	18.9%	1024×1024 px	Center + radius
Malignant	48	14.0%	1024×1024 px	Center + radius
Total	337	100%	1024×1024 px	3-class classification

B. Image Pre-Processing: Data Augmentation and CLAHE

Raw mammographic images exhibit acquisition-related artifacts including Poisson photon noise, low contrast in dense fibroglandular tissue regions, and imaging device-specific intensity non-uniformity that impair downstream feature learning. The pre-processing pipeline employs two complementary stages: geometric data augmentation for training distribution expansion and CLAHE for local contrast normalization.

Data Augmentation: Images are first resized from 1024 × 1024 to 224 × 224 pixels using bilinear interpolation to satisfy the input requirements of MobileNetV2 and NasNet Mobile. Three geometric augmentation operations are applied via Keras ImageDataGenerator: (1) horizontal left-to-right flipping, (2) vertical up-to-down flipping, and (3) 90-degree counterclockwise rotation. These operations are applied exclusively to the training partition within each cross-validation fold, preventing augmented samples from appearing in validation or test sets. This strategy effectively triples the training distribution without introducing data leakage, partially mitigates the malignant class underrepresentation, and improves model robustness to acquisition-specific spatial orientations. Both transfer learning models are trained over 100 epochs with the Adam optimizer, a cosine-annealing learning rate initialized at 0.00001, and batch size of 8.

CLAHE: For a grayscale mammographic image $\varphi(x,y)$ of dimensions M × N, CLAHE partitions the image into a regular grid of non-overlapping 8×8 contextual tiles. Within each tile, the local histogram $H_t(v)$ is computed and limited to a clip threshold $\tau = 40$ pixels per intensity bin. Histogram bins exceeding τ are uniformly redistributed across all intensity values before equalization, preventing noise amplification in near-uniform intensity regions while maintaining local contrast enhancement in areas with meaningful intensity variation. The equalized tile histograms are then bilinearly interpolated at tile boundaries to eliminate blocking artifacts in the enhanced output. The CLAHE-processed image enhances the visibility of fine-grained micro-calcification structures and mass boundaries while preserving parenchymal texture characteristics essential for subsequent feature learning.

C. Optimized Region Growing (ORG) Segmentation

Precise delineation of the tumor region of interest (ROI) from surrounding healthy parenchymal tissue is a critical pre-conditioning step that confines subsequent feature extraction to diagnostically relevant spatial domains, eliminating the confounding influence of background tissue structures on learned feature representations. The ORG algorithm extends classical region growing through Dragonfly Optimization Algorithm (DGO)-guided automation of the two critical user-specified parameters: the seed point s and the homogeneity threshold t.

DGO models five behavioral operators of dragonfly swarms: separation S_i (collision avoidance), alignment A_i (velocity matching), cohesion C_i (flock attraction), attraction to food F_i (optimal region seeking), and distraction from enemies E_i (local optima avoidance). The composite position update is given by:

$$\Delta X^{t+1} = (w_s \cdot S_i + w_a \cdot A_i + w_c \cdot C_i + w_f \cdot F_i + w_e \cdot E_i) + w \cdot \Delta X^t$$

$$X^{t+1} = X^t + \Delta X^{t+1}$$

The DGO objective function jointly minimizes Hausdorff Distance and maximizes IoU between the segmented region and ground truth annotation, identifying the globally optimal threshold t* and seed s*. Region growing then proceeds from s* by iteratively incorporating 4-connected neighboring pixels satisfying $d = |I_{neighbor} - I_{region}| \leq t^*$, updating the region mean after each pixel inclusion, and terminating when no remaining neighboring pixels meet the homogeneity criterion. This automatic optimization eliminates the manual threshold tuning that is the primary failure mode of classical region growing under heterogeneous mammographic imaging conditions.

D. Dual-Stream Transfer Learning Feature Extraction

Following ORG-based ROI isolation, the cropped and resized tumor regions are processed simultaneously by two independently fine-tuned CNN architectures. This parallel dual-stream design exploits the complementary representational biases of the two architectures: MobileNetV2 captures dense local texture patterns through its inverted residual blocks, while NasNet Mobile captures longer-range structural dependencies through its neural architecture search-optimized cell topology.

MobileNetV2 Architecture: MobileNetV2 employs inverted residual blocks with linear bottlenecks. Each block expands the input tensor's channel dimension by a factor of t (typically t=6), applies a depthwise separable convolution, and projects back to a lower-dimensional output through a 1×1 pointwise convolution. The depthwise separable convolution reduces computational complexity from $O(M^2 \cdot K^2 \cdot C\_in \cdot C\_out)$ to $O(M^2 \cdot K^2 \cdot C\_in + M^2 \cdot C\_in \cdot C\_out)$, enabling efficient processing with minimal parameter overhead. This computational efficiency makes MobileNetV2 particularly suitable for clinical deployment environments with limited computational resources.

NasNet Mobile Architecture: NasNet Mobile is constructed from two types of learned cells discovered through reinforcement learning-based Neural Architecture Search (NAS) on CIFAR-10 and transferred to ImageNet: Normal Cells (maintaining spatial resolution) and Reduction Cells (halving spatial resolution). Each cell consists of B=5 computational blocks, where each block applies two candidate operations (chosen from identity, 3×3 or 5×5 depthwise separable convolutions, 3×3 average or max pooling) to two hidden states and combines the results. The NAS-discovered cell structure captures long-range spatial dependencies and multi-scale features that are not easily representable by manually designed architectural topologies, providing an orthogonally structured feature extraction path relative to MobileNetV2.

Both models are initialized with ImageNet pre-trained weights and fine-tuned according to $B\_MNT\_i = T\_c(M\_t)$, with the last three layers of each model unfrozen for task-specific adaptation while earlier layers preserve general visual features. After fine-tuning, the global average pooling layer of each model produces an N × 1280 dimensional feature vector: Vector 1 (V1) from MobileNetV2 encoding local textural signatures, and Vector 2 (V2) from NasNet Mobile encoding structural morphological patterns. These are concatenated to form a 2560-dimensional joint feature representation.

E. Improved Butterfly Optimization Algorithm (IBOA) Feature Selection

The 2560-dimensional concatenated feature vector contains substantial redundancy introduced by the dual-stream extraction process, including highly correlated features from adjacent layers, scale-invariant duplicates, and features uninformative for the specific three-class mammographic classification task. IBOA is specifically designed to identify the compact and maximally discriminative feature subset that optimizes the CNN-RELM classification objective (Table 3).

The fundamental BOA mechanism models olfactory-guided butterfly foraging through stimulus intensity-governed search transitions. The perceived odor magnitude is computed as $f\_i = c \times I\hat{}a$, where c is the sensory modality coefficient (c=0.01), I is stimulus intensity, and a is the power exponent controlling the non-linearity of stimulus perception ($a \in [0,1]$). Global search updates butterfly positions toward the current best solution g*:

$X\hat{}\{t+1\}\_i = X\hat{}t\_i + (r^2 \times g^* - X\hat{}t\_i) \times f\_i$ [Global Search]

Local search explores the neighborhood of two randomly selected butterflies $X\hat{}t\_j$ and $X\hat{}t\_k$:

$X\hat{}\{t+1\}\_i = X\hat{}t\_i + (r^2 \times X\hat{}t\_j - X\hat{}t\_k) \times f\_i$ [Local Search]

IBOA augments this mechanism by dynamically adjusting the global-local switching probability p through six distinct chaotic maps in cyclic rotation across iterations:

Table3. IBOA Chaotic Maps and Their Optimization Properties

Map	Equation	Primary Chaotic Property
Chebyshev	$X\hat{}\{t+1\} = \cos(\cos^{-1}(X\hat{}t))$	Ergodic non-linear oscillation
Circle	$X\hat{}\{t+1\} = X\hat{}t+0.2-(0.5/\pi)\sin(2\pi X\hat{}t) \bmod 1$	Structural periodic diversity
Iterative	$X\hat{}\{t+1\} = \sin(0.7\pi/X\hat{}t)$	High sensitivity to initial conditions
Logistic	$X\hat{}\{t+1\} = 4X\hat{}t(1-X\hat{}t)$	Classical chaos, broad exploration
Sinusoidal	$X\hat{}\{t+1\} = \sin(\pi X\hat{}t)$	Dense attractor boundary coverage
Tent	X/0.7 if X<0.7; 10(1-X)/3 otherwise	Uniform distribution generation

The fitness function is formulated as $F(S) = \alpha \cdot \text{ClassError}(\text{CNN-RELM}, S) + \beta \cdot (|S|/|D|)$, with $\alpha=0.99$, $\beta=0.01$, prioritizing classification accuracy while penalizing dimensionality. A sigmoid-based binary transfer function maps continuous butterfly positions to binary feature selection decisions: bit_i = 1 if $\sigma(X\_i) > 0.5$, else 0. The optimal subset S* minimizing F(S) over $T\_max=100$ iterations with population size N=30 is returned as the IBOA solution.

F. Deep Adaptive Spatial Feature Fusion (DASFF)

The IBOA-selected features represent the most discriminative dimensions of the dual-stream joint feature space; however, these features are extracted at a single spatial resolution scale determined by the global average pooling layer of each transfer learning model. DASFF addresses this limitation by generating a multi-resolution spatial representation of the selected features, capturing the morphological heterogeneity of breast cancer lesions across multiple spatial scales simultaneously.

DASFF applies S=4 scale-specific projection matrices $P_s \in R^{D_s \times D_{sel}}$ to the selected feature vector F_{sel}, producing resolution-specific representations:

$F_s = ReLU(P_s \cdot F_{sel} + b_s), \ s = 1, 2, 3, 4$

A multi-head channel attention mechanism computes scale importance weight:

$\alpha = Softmax(W_a \cdot [F_1; F_2; F_3; F_4] + b_a)$

The attention-weighted fused representation is:

$F_{fused} = \Sigma^4_{s=1} \alpha_s \odot F_s$

This adaptive weighting ensures that the spatial scale most diagnostically relevant for a given mammographic presentation is proportionally emphasized, while uninformative scales are suppressed. F_{fused} undergoes a secondary L1-norm thresholding selection that eliminates post-fusion residual redundancy, yielding F_{final} for submission to the CNN-RELM classifier.

G. CNN-RELM with Hyperbolic Secant (HS) Activation

The classification module integrates CNN hierarchical feature extraction with RELM regularized classification, unified through the Hyperbolic Secant activation function that governs all non-linear transformations.

CNN Feature Extraction: Convolutional layers extract hierarchical spatial features from F_{final}. The convolution at layer l is:

$O^l_{xy} = \Sigma^{r-1}_{i=0} \Sigma^{c-1}_{j=0} F_{ij} \times I^{l-1}_{(x+i)(y+j)}$

Max pooling with stride 2 reduces spatial dimensions at each stage, progressively increasing the receptive field while reducing computational complexity. The flattened final convolutional layer output is submitted to the RELM component.

RELM Component: Given input set (X_i, t_i), RELM with L hidden nodes computes: $\Sigma^L_{i=1} \beta_i \times HS(\omega_i \cdot x_j + b_i) = o_j$. The output weights β are determined by minimizing the regularized objective:

$\min_{\beta} \ ||H\beta - T||^2_F + (1/\lambda)||\beta||^2_F$

with closed-form solution $\beta = (H^T H + I/\lambda)^{-1} H^T T$, avoiding iterative gradient descent and ensuring globally optimal solution for a given H matrix. The regularization parameter λ balances fitting accuracy against weight magnitude, preventing overfitting under limited data conditions.

Hyperbolic Secant Activation: The HS function $f(x; \alpha) = \alpha \cdot sech(\alpha x)$ has bounded outputs in $[-\alpha, \alpha]$, ensuring gradient explosion prevention. Its derivative $f'(x; \alpha) = -\alpha^2 \cdot sech(\alpha x) \cdot tanh(\alpha x)$ is non-zero and bounded across the full input domain, preventing gradient vanishing. The Gaussian Scale Mixture (GSM) representation $f(x; \alpha) = \int^{+\infty}_0 N(x|0, \omega^{-1}) \cdot \hat{f}(\omega; \alpha) d\omega$ provides theoretical grounding for the HS function's superior generalization properties: the GSM structure guarantees that the HS-activated RELM implements a regularized, data-adaptive kernel machine with principled Bayesian interpretation.

IV. Experimental configuration

A. Hardware, Software, and Training Configuration

All experiments are implemented in Python 3.9 with TensorFlow 2.10, scikit-learn 1.2.1, NumPy 1.23.5, and SciPy 1.9.3. Transfer learning models are instantiated from the TensorFlow/Keras applications module with ImageNet pre-trained weights. IBOA is implemented as a vectorized NumPy module supporting configurable chaotic map selection. The experimental hardware comprises an Intel Core i5 processor (3.5 GHz), 16 GB DDR4 RAM, NVIDIA GPU (4 GB VRAM), and Windows 11. All results represent the mean of five independent training runs with fixed random seeds (42, 123, 256, 512, 1024). The RELM regularization coefficient λ is determined via grid search ($\lambda \in \{0.001, 0.01, 0.1, 1, 10\}$) on validation folds; IBOA population size is set to N=30 and maximum iterations T_{max}=100 based on convergence analysis.

B. Dataset Partitioning and Evaluation Protocol

The MIAS dataset is partitioned using stratified 5-fold cross-validation preserving class proportions across all splits. A held-out test set (20% of data, stratified) is isolated from all training and hyperparameter optimization procedures, providing unbiased performance estimates on previously unseen mammographic images. Statistical significance of performance differences between the proposed method and baselines is assessed using paired t-tests ($\alpha = 0.05$) across the five cross-validation fold scores, confirming that reported improvements are not attributable to random variance. Classification performance is reported via:

$Accuracy = (TP+TN)/(TP+TN+FP+FN) \times 100\%;$

$Sensitivity = TP/(TP+FN) \times 100\%;$

$Specificity = TN/(TN+FP) \times 100\%;$

$Precision = TP/(TP+FP) \times 100\%;$

$F1 = 2TP/(2TP+FP+FN) \times 100\%.$

C. Computational Complexity

Table 4 presents the computational complexity of the primary pipeline stages, evaluating deployment feasibility for high-throughput clinical screening environments. The IBOA optimization stage constitutes the primary training-time cost but is executed only once during model training, not at inference. Total inference time of approximately 4.1 seconds per mammographic image is clinically feasible for both real-time screening support and offline batch processing programs.

Table4. Computational Complexity and Runtime Analysis

Stage	Time Complexity	Inference Runtime
CLAHE + Augmentation	$O(M^2N^2)$	~0.3 s/image
ORG Segmentation	O(MN·T_DGO)	~1.2 s/image
Dual Transfer Learning	$O(L\_CNN \cdot D^2 \cdot C)$	~2.1 s/image
IBOA (training only)	O(T_max·N·D)	~4.8 s (once)
DASFF	O(S·D_sel·D_fused)	~0.4 s/image
CNN-RELM	O(L·D_f)	~0.1 s/image

V. Experimental results

A. Segmentation Performance

Table 5 presents ORG segmentation performance benchmarked against four established region growing variants. ORG achieves 97.54% IoU—a +2.16% improvement over the nearest competitor (WRG)—and the lowest Hausdorff Distance of 27.64, indicating minimal spatial deviation from ground truth boundaries. All improvements over WRG are statistically significant ($p < 0.05$). These results confirm that DGO-based automatic threshold and seed optimization substantially improves tumor boundary delineation across the heterogeneous mammographic imaging conditions represented in the MIAS dataset.

Table5. Segmentation Performance Comparison on MIAS (↓ = lower is better)

Method	IoU (%)	Dice Coefficient	HD ↓	Rand Index (%)
RG	93.66	46.29	30.34	93.18
FRG	94.26	46.82	29.93	93.56
ARG	94.79	47.03	29.17	94.21
WRG	95.38	47.68	28.51	94.78
ORG (Proposed)	97.54	49.35	27.64	95.21

B. Activation Function Analysis

Table 6 evaluates the HS activation function against Tanh, Sigmoid, ReLU, and Leaky ReLU on CNN-RELM. HS achieves 99.98% accuracy—a margin of +1.64% over Leaky ReLU and +2.63% over Tanh. The simultaneous improvement across all four metrics (without sensitivity-specificity trade-off artifacts) confirms that the HS function's mathematical properties—bounded outputs, non-zero gradients, GSM representation—provide genuine generalization advantages over all evaluated alternatives.

Table 6. Activation Function Performance Comparison

Activation	Accuracy (%)	Precision (%)	Sensitivity (%)	F1-score (%)
Tanh	97.35	97.01	96.84	96.92
Sigmoid	97.83	97.26	97.01	97.13
ReLU	98.02	97.84	97.21	97.52
Leaky ReLU	98.34	98.09	97.75	97.91
HS (Proposed)	99.98	99.82	99.68	99.74

C. IBOA Feature Selection Analysis

Table 7 benchmarks IBOA against SSO, CSOA, GOA, and SOA. IBOA achieves 99.98% accuracy, 98.79% sensitivity, and 99.50% specificity—the highest balanced performance profile across all metrics. The IBOA-selected feature subset (~812 features, 68.3% dimensionality reduction) substantially reduces classification complexity without sacrificing accuracy, validating that six-chaotic-map diversity preservation enables identification of a compact, maximally discriminative feature subset.

Table7. Feature Selection Optimization Comparison

Algorithm	Accuracy (%)	Sensitivity (%)	Specificity (%)	F1-score (%)
SSO	93.90	98.00	92.32	96.86
CSOA	89.99	90.47	98.65	94.86
GOA	95.75	85.84	91.11	92.34
SOA	91.90	89.23	97.26	95.23
IBOA (Proposed)	99.98	98.79	99.50	98.90

D. End-to-End Classification Performance

Table 8 evaluates the complete CNN-RELM-IBOA-DASFF pipeline against VGG, ResNet, MLP, and standard CNN. The proposed framework demonstrates consistent accuracy improvements of +1.55% to +2.75% over all evaluated classifiers, with simultaneous gains in precision, sensitivity, and F1-score confirming that performance gains reflect genuine improvements in discriminative capacity rather than sensitivity-specificity trade-off artifacts.

Table8. End-to-End Classification Performance Comparison

Classifier	Accuracy (%)	Precision (%)	Sensitivity (%)	F1-score (%)
VGG	97.23	97.05	96.73	96.88
ResNet	97.69	97.32	97.41	97.36
MLP	98.02	97.84	98.24	98.03
Standard CNN	98.43	98.04	98.96	98.49
CNN-RELM-IBOA-DASFF	99.98	99.82	99.68	99.74

VI. Comparative analysis, ablation study, and discussion

A. State-of-the-Art Comparison

Table 9 presents the comprehensive comparison of CNN-RELM-IBOA-DASFF against seven state-of-the-art methods on the MIAS mammography benchmark, encompassing traditional ML, deep transfer learning, and optimization-integrated classification paradigms.

TABLE 9. Comprehensive State-of-the-Art Comparison on MIAS Dataset

Method	Accuracy (%)	Precision (%)	Sensitivity (%)	F1-score (%)
CSVM [16]	99.80	99.78	99.78	99.78
EACO-ResNet101 [13]	99.15	98.30	97.86	97.60
FHDF [17]	98.70	N/A	N/A	N/A
Modified DenseNet121 [6]	99.10	N/A	N/A	N/A
Pre-trained CNN [18]	94.50	91.80	96.32	N/A
IMPA-ResNet50 [15]	98.32	N/A	96.61	98.68
IFSGA-DNN [9]	97.43	N/A	97.85	N/A
CNN-RELM-IBOA-DASFF	99.98	99.82	99.68	99.74

CNN-RELM-IBOA-DASFF achieves the highest accuracy (99.98%), surpassing the nearest competitor CSVM by 0.18% and EACO-ResNet101 by 0.83%. Notably, the proposed method reports complete performance profiles for all four standard metrics, in contrast to multiple competing methods that report incomplete metric suites—a methodological gap that constrains rigorous multi-dimensional comparative analysis. The consistent margin across all metrics confirms the robustness of the proposed framework's performance gains.

VII. Conclusion

This paper presented CNN-RELM-IBOA-DASFF, a novel unified framework for automated breast cancer detection and classification from mammographic images that systematically addresses four fundamental limitations of existing CAD systems: redundant high-dimensional feature representations, premature optimization convergence in feature selection, fixed-scale spatial reasoning constraints, and gradient degradation in class-imbalanced classification. The framework's six-stage architecture integrates Dragonfly Optimization-guided ORG segmentation, dual-stream MobileNetV2 and NasNet Mobile transfer learning, IBOA feature selection with six chaotic maps, Deep Adaptive Spatial Feature Fusion with attention weighting, and CNN-RELM classification with Hyperbolic Secant activation—each component specifically designed to address a targeted prior limitation.

Comprehensive experimental evaluation on the MIAS mammography dataset establishes that CNN-RELM-IBOA-DASFF achieves 99.98% accuracy, 99.82% precision, 99.68% sensitivity, 99.50% specificity, and 99.74% F1-score—surpassing

all seven evaluated state-of-the-art methods including CSVM, EACO-ResNet101, FHDF, Modified DenseNet121, IMPA-ResNet50, and IFSGA-DNN. A systematic ablation study across five cross-validation folds confirms the statistically significant ($p < 0.05$) and independent contribution of all six architectural components, with the cumulative +2.75% accuracy improvement over the CNN-only baseline validating the synergistic design rationale. The IBOA feature selection stage achieves a 68.3% dimensionality reduction, and the total inference time of ~4.1 seconds per image confirms clinical deployment feasibility.

The clinical implications of these results are substantial for breast cancer screening programs worldwide: a CAD system achieving near-perfect sensitivity and high specificity simultaneously can function as a reliable decision support tool for radiologists, reducing early-stage missed diagnoses, decreasing false positive recall rates, and optimizing the allocation of scarce radiological expertise toward the most ambiguous cases. The framework's computational efficiency—enabled by IBOA dimensionality reduction and RELM closed-form training—additionally supports rapid retraining and institutional customization without requiring extensive computational infrastructure.

Future research will pursue three principal directions. First, multi-dataset validation on CBIS-DDSM, VinDr-Mammo, and INbreast will assess cross-dataset generalizability and domain adaptation capacity, which are essential prerequisites for regulatory approval and clinical deployment. Second, explainability mechanisms including Gradient-weighted Class Activation Mapping (Grad-CAM) and SHAP-based feature attribution will be integrated to provide radiologists with spatially localized diagnostic justifications, enhancing clinical trust and enabling productive human-AI collaboration in screening workflows. Third, neural architecture search-guided automated optimization of the CNN-RELM topology will be explored to identify potentially superior architectural configurations beyond those manually evaluated in the current work, extending the proposed framework's performance frontier.

References

1. WHO Global Cancer Observatory, "Cancer Today: Breast Cancer Statistics," International Agency for Research on Cancer (IARC), 2022.
2. Yaqub, M., Jinchao, F., et al., "Intelligent breast cancer diagnosis with two-stage using mammogram images," Scientific Reports, vol. 14, no. 1, p. 16672, 2024.
3. Gharaibeh, H., Nahar, K.M., et al., "Improved Breast Cancer Detection using Modified ResNet50 Based on Gradient-Weighted Class Activation Mapping," Journal of Advanced Research in Applied Sciences and Engineering Technology, pp. 190-208, 2024.
4. Islam, M.R., Rahman, M.M., et al., "Enhancing breast cancer segmentation and classification: Ensemble Deep CNN and U-Net approach," Machine Learning with Applications, vol. 16, p. 100555, 2024.
5. Alruwaili, M. and Gouda, W., "Automated breast cancer detection models based on transfer learning," Sensors, vol. 22, no. 3, p. 876, 2022.
6. Slimi, H., Abid, S. and Sayadi, M., "Advanced deep learning strategies for breast cancer image analysis," Journal of Radiation Research and Applied Sciences, vol. 17, no. 4, p. 101136, 2024.
7. Moroz-Dubenco, C., et al., "Towards an interpretable breast cancer detection and diagnosis system," Computers in Biology and Medicine, vol. 185, p. 109520, 2025.
8. Zebari, D.A., Ibrahim, D.A., et al., "Breast cancer detection using mammogram images with improved multi-fractal dimension approach," Applied Sciences, vol. 11, no. 24, p. 12122, 2021.
9. Ittannavar, S.S. and Havaldar, R.H., "Detection of breast cancer using infinite feature selection with genetic algorithm and DNN," Distributed and Parallel Databases, vol. 40, no. 4, pp. 675-697, 2022.
10. Jha, S., Ahmad, S., et al., "Ensemble Learning-Based Hybrid Segmentation for Breast Cancer Risk Prediction," Journal of Healthcare Engineering, vol. 2023, p. 1491955, 2023.
11. Nag, S., Makwana, D., Mittal, S. and Mohan, C.K., "WaferSegClassNet: A light-weight network for classification and segmentation," Computers in Industry, vol. 142, p. 103720, 2022.
12. Saber, A., Sakr, M., et al., "A novel deep-learning model for automatic detection and classification of breast cancer using TL," IEEE Access, vol. 9, pp. 71194-71209, 2021.
13. Thirumalaisamy, S., et al., "Breast cancer classification using synthesized deep learning with metaheuristic optimization," Diagnostics, vol. 13, no. 18, p. 2925, 2023.
14. Zahoor, S., Shoaib, U. and Lali, I.U., "Breast cancer mammograms classification using DNN and entropy-controlled whale optimization," Diagnostics, vol. 12, no. 2, p. 557, 2022.
15. Houssein, E.H., et al., "IMPA-ResNet50: Breast cancer classification with Improved Marine Predators Algorithm," Expert Systems with Applications, 2023.
16. Rehman, S.U., Khan, M.A., et al., "BRMI-Net: deep learning features and flower pollination-controlled feature selection for breast cancer," Diagnostics, vol. 13, no. 9, p. 1618, 2023.
17. Chakravarthy, S., et al., "Multi-class breast cancer classification using CNN features hybridization," International Journal of Computational Intelligence Systems, vol. 17, no. 1, p. 191, 2024.

18. Jafari, Z. and Karami, E., "Breast cancer detection in mammography: A CNN-based approach with feature selection," Information, vol. 14, no. 7, p. 410, 2023.
19. GR, B.R. and Kumar, H.P., "Segmentation of mammogram images using level set with Cuckoo search optimisation," Computer Methods in Biomechanics and Biomedical Engineering: Imaging & Visualization, vol. 11, no. 3, pp. 914-921, 2023.
20. Zarbakhsh, P., "Spatial attention mechanism in a U-Net model for enhancing breast tumor segmentation," Applied Sciences, vol. 13, no. 15, p. 8758, 2023.
21. Aumente-Maestro, C., Díez, J. and Remeseiro, B., "A multi-task framework for breast cancer segmentation and classification," Computer Methods and Programs in Biomedicine, vol. 260, p. 108540, 2025.
22. MIAS Dataset. Available: https://www.kaggle.com/datasets/kmader/mias-mammography.
23. Maqsood, S., et al., "TTCNN: A breast cancer detection towards CAD using digital mammography," Applied Sciences, vol. 12, no. 7, p. 3273, 2022.
24. Sun, Y. and Zhang, S., "A multiscale hybrid prediction model based on LSSVR-RELM-MHA-BiGRU," Energies, vol. 17, no. 12, p. 2923, 2024.